



Research Paper

Tuning Ni-catalyzed CO₂ hydrogenation selectivity via Ni-ceria support interactions and Ni-Fe bimetallic formationLea R. Winter^a, Elaine Gomez^a, Binhang Yan^b, Siyu Yao^b, Jingguang G. Chen^{a,b,*}^a Department of Chemical Engineering, Columbia University, New York, NY 10027, United States^b Chemistry Department, Brookhaven National Laboratory, Upton, NY 11973, United States

ARTICLE INFO

Keywords:

CO₂ reduction

Ni loading

Ni-Fe bimetallic catalysts

Metal oxide

XANES

ABSTRACT

CO₂ hydrogenation over Fe-modified Ni/CeO₂ catalysts was investigated in a batch reactor using time-resolved *in situ* FTIR spectroscopy. Low loading of Ni/CeO₂ was associated with high selectivity to CO over CH₄, while higher Ni loading improved CO₂ hydrogenation activity with a reduced CO selectivity. X-ray absorption near-edge structure (XANES) analysis revealed Ni to be metallic for all catalysts including the CO-selective low loading 0.5% Ni catalyst, suggesting that the selectivity trend is due to structural rather than oxidation state effects. The loading amount of 1.5% Ni was selected for co-impregnation with Fe, based on the significant shift in product selectivity towards CH₄ for that loading amount, in order to shift the selectivity towards CO while maintaining high activity. Temperature programmed reduction (TPR) results indicated bimetallic interactions between Ni and Fe, and XANES analysis showed that about 70% of Fe in the bimetallic catalysts was oxidized. The Ni-Fe catalysts demonstrated improved selectivity towards CO without significantly compromising activity, coupling the high activity of Ni catalysts and the high CO selectivity of Fe. The general trends in Ni loading and bimetallic modification should guide efforts to develop non-precious metal catalysts for the selective production of CO by CO₂ hydrogenation.

1. Introduction

Catalytic conversion of CO₂ to chemicals and fuels represents a crucial process for managing the anthropogenic environmental footprint. The search for impactful CO₂ mitigation strategies has become urgent because of the current unprecedented rise in atmospheric CO₂ levels and associated ocean acidification [1,2]. In 2012 alone, the EPA estimated that climate and weather disasters linked to anthropogenic climate change cost the US economy over \$100 billion [3]. Moreover, the anticipated increase in US reliance on coal necessitates enhanced CO₂ mitigation strategies in order to meet regulations for “clean” burning of coal [4]. Compared to other carbon capture, utilization, and storage (CCUS) technologies, the conversion of CO₂ to fuels and chemicals provides a potentially more effective means of circulating carbon and alleviating the effects of climate change than does sequestration [5–7]. Catalytic conversion of CO₂ is an indispensable technology for the renewable energy portfolio given the projected 30% increase in global energy demand from 2020 to 2040 [8].

CO₂ can be catalytically converted into CO, which serves as a feedstock for producing chemicals and fuels via Fischer-Tropsch synthesis. For example, annual olefin production is in the order of 200

Mt, and each ton of olefin produced emits 1.2–1.8 tons of CO₂ [9]. Thus, closing the carbon loop by manufacturing these products with a CO₂ feedstock via conversion to CO has the potential to substantially reduce the net CO₂ emissions associated with olefin production [10]. A net reduction of CO₂ should be achieved if H₂ is produced from CO₂-free methods such as water electrolysis with electrons derived from renewable energy.

Catalytic CO₂ reduction using hydrogen can produce CO, CH₄, and CH₃OH [10]. Although methanol appears to represent a desirable option for CO₂ utilization, the impact on CO₂ consumption is limited to lower than 0.1% for global reduction of CO₂ emissions [11]. Natural gas production in the US is projected to increase by 2040 to a point where 21% of collected natural gas will be allocated as exports [8]. Given the abundance of CH₄, one of the challenges for CO₂ hydrogenation is the selective conversion of CO₂ to CO instead of CH₄.

The most widely accepted mechanism describing reduction of CO₂ by H₂ consists of hydrogenation of CO₂ into an oxygenate intermediate followed by cleavage of the C=O bond [10,12]. Metal nanoparticles supported on reducible metal oxides are generally employed as “dual functional” catalysts [10]: (1) reducible oxides adsorb CO₂ via oxygen vacancies and (2) dispersed metal active sites readily dissociate

* Corresponding author at: Department of Chemical Engineering, Columbia University, New York, NY 10027, United States.
E-mail address: jgchen@columbia.edu (J.G. Chen).

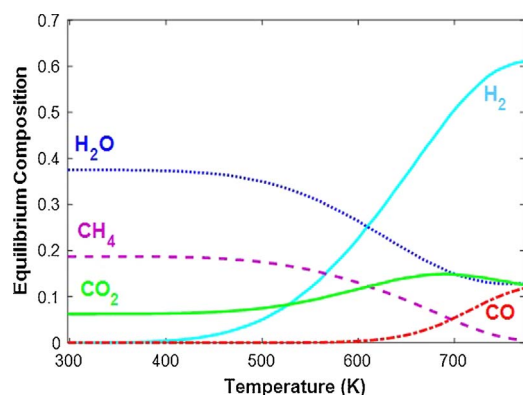
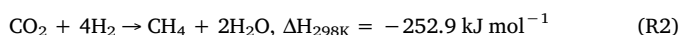
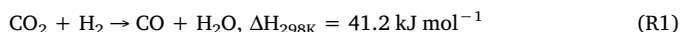


Fig. 1. Thermodynamic equilibrium composition for hydrogenation of CO₂ at 10 Torr with an initial molar H₂:CO₂ ratio of 3:1 (calculated using HSC Chemistry 6.0).

hydrogen, allowing reactive atomic hydrogen to spill over onto the support and hydrogenate the CO₂ that is adsorbed on the oxides [12–15]. More recent studies have also identified the importance of oxide-metal interfaces in the initial activation of CO₂ [16]. As summarized recently, theoretical and experimental investigations have demonstrated that the most likely mechanism for hydrogenation of CO₂ to CH₃OH and CH₄ proceeds either via a CO intermediate that is subsequently hydrogenated, or along the formate pathway [10,17]. CO may be released as a gaseous product via the reverse water gas shift (RWGS) pathway (R1), or CO can serve as an adsorbed intermediate that is further hydrogenated to CH₄ (overall reaction, (R2)) [18–21].



The equilibrium distribution of products for CO₂ reduction using hydrogen, shown in Fig. 1, demonstrates the thermodynamic preference of CH₄ production, in particular at low temperatures. A major challenge for effective utilization of CO₂ lies in the design of a dual functional catalyst to actively and selectively hydrogenate CO₂ to CO at low temperatures.

The most promising and well-studied non-precious metal catalysts for CO₂ methanation are Ni-based catalysts with relatively high Ni loadings [10,22,23]. Although oxide-supported Ni catalysts are selective towards CO at very low metal loading, the low Ni loading leads to low CO₂ conversion. An ideal RWGS catalyst must have strong activity for hydrogenation and C=O bond scission, but an active catalyst with these functionalities may over-hydrogenate CO and produce CH₄. This study aims to modify oxide-supported Ni catalysts with Fe in order to take advantage of the high activity of non-precious Ni metal while optimizing selectivity towards CO.

In the current study, CeO₂ was chosen as the metal oxide support because of its reducibility to produce oxygen vacancies, its capacity to facilitate bimetallic bond formation [24,25], and its tendency to have strong metal-support interactions (SMSIs) with Ni [26]. CeO₂-supported Ni particles are selective to CO in the RWGS reaction, but CH₄ has been observed for Ni loading > 3 wt% [27–31]. Low Ni loading has been linked to enhancement of the oxygen adsorption capacity of CeO₂ following catalyst reduction [32,33], and higher Ni loading is associated with aggregation of Ni particles [29,34,35]. Extensive studies of CeO₂-supported Ni catalysts have revealed vast differences in the structural, electronic, and mechanistic properties of the catalysts according to the Ni loading, dispersion, and particle sizes because of SMSIs [30,31,36,37].

The current study first compares the CO selectivity at different Ni loadings on CeO₂ in order to determine the loading threshold for controlling the CO₂ hydrogenation reaction selectivity. After identifying the Ni loading for which CH₄ production becomes significant, modification of this catalyst with Fe was investigated as a strategy for

shifting the reaction selectivity towards CO while retaining the high activity associated with higher Ni content. Bimetallic catalysts of Fe and Ni often have been found to exhibit similar properties to precious metal catalysts in reforming [38,39], hydrogenation [40], water-gas shift [41,42], and CO oxidation reactions [43,44]. Overall, bimetallic catalysts have often shown enhanced hydrogenation activity and selectivity over their parent metals [39–42]. This study aims to probe the ability of Fe to modify the electronic properties of CeO₂-supported Ni catalysts in order to shift the reaction pathway towards CO selectivity at comparatively high CO₂ hydrogenation activity.

2. Experimental

2.1. Catalyst preparation

All catalysts were synthesized using incipient wetness impregnation over commercially obtained CeO₂ (35–45 m²/g cubic, Sigma-Aldrich) supports. Precursor salts of Ni(NO₃)₂·6H₂O (Alfa Aesar) and Fe(NO₃)₃·9H₂O (Alfa Aesar) were dissolved in an amount of water below the capacity for filling the pores of 3 g of CeO₂. The precursor solution was added dropwise to the support powder and mixed thoroughly between droplets. This solution was then dried at 363 K for > 12 h and calcined at 563 K for 2 h. The bimetallic catalysts were synthesized using co-impregnation from a solution containing both precursors. Admetal loading amounts were determined using weight percent, referred to as percent in the current paper.

2.2. Catalyst characterization

2.2.1. Pulse CO chemisorption and temperature-programmed reduction (TPR)

Pulse CO chemisorption was performed using an AMI-200ip (Altamira) as described previously [45] in order to determine the number of active sites on the catalysts. TPR measurements were used to characterize the reduction behavior of the catalysts. About 200 mg of catalyst were loaded into a U-shaped quartz tube, and the samples were reduced with 20 mL min^{−1} of 10% H₂ in Ar at 723 K for 0.5 h with a ramp rate of 14 K min^{−1}. The amount of H₂ consumed was quantified using a thermal conductivity detector (TCD) for TPR measurements. The samples were cooled in inert atmosphere to room temperature before pulsing CO. The amount of CO flowing out of the reactor was measured using a TCD. The amount of CO adsorbed provided a quantitative measure of the number of active sites for a given catalyst.

2.2.2. Powder X-ray diffraction (XRD) and transmission electron microscopy (TEM)

XRD patterns were collected using a PANalytical X'Pert³ Powder XRD system with a Cu Kα X-ray source. Samples were scanned between 20° to 80° 2θ with a 0.2188° s^{−1} scan speed. The catalysts with the lowest (0.5%) and highest (5%) Ni loadings were compared, in addition to blank CeO₂ that was treated by incipient wetness impregnation with a blank water solution.

HR-TEM imaging was conducted using a JEOL2100F TEM operated at 200 kV. Samples were prepared by reducing in H₂ and using the drop-cast method. Particle size distributions were obtained by measuring particle area in ImageJ Software for several different images of each catalyst and assuming a spherical geometry to obtain diameter.

2.2.3. X-ray absorption near edge structure (XANES)

XANES measurements of Ni and Fe K-edges were performed in order to determine the oxidation states of the respective metals in the catalysts. The experiments were completed at beamline 2-2 of the Stanford Synchrotron Radiation Lightsource (SSRL), SLAC National Accelerator Laboratory. Samples were prepared by pressing the powder catalysts into pellets and sieving to 60–80 mesh. The catalysts were reduced in a mixture of H₂ and He at 723 K, and spectra were recorded at the

reduction temperature in a custom-designed, *in situ* microchannel reactor cell [46]. After the reduction step using H₂ and He at 723 K, the Ni catalysts were cooled to 623 K and a reaction mixture of 3 H₂:1 CO₂ with He as inert diluent was introduced at a flow rate below 15 mL min⁻¹. All spectra were collected in the fluorescence mode using a 13-channel Ge detector. The XANES spectra of metal and metal oxide standards were collected in the transmission mode as references

2.3. Reactor studies using *in situ* FTIR spectroscopy

Experiments were conducted in a batch reactor and gas-phase concentrations were monitored using a Fourier transform infrared (FTIR) Thermo Nicolet Nexus 470 spectrometer equipped with a mercury cadmium telluride (MCT-A) detector [45]. Spectra were recorded with 4 cm⁻¹ resolution every 30 s, with 32 scans collected and averaged for each spectrum. Time-resolved gas-phase spectra were collected during reactions to monitor reactant and product species. The species concentrations were estimated using the absorbance intensities of their characteristic vibrational modes as follows: $\nu(\text{C}=\text{O})$ at 2357 cm⁻¹ for CO₂, $\nu(\text{C}=\text{O})$ at 2172 cm⁻¹ for CO, $\delta(\text{H}-\text{O}-\text{H})$ at 1559 cm⁻¹ for H₂O, and $\nu(\text{C}-\text{H})$ at 3016 cm⁻¹ for CH₄. Intensities were converted to concentrations by calibrating for each species, correlating vibrational absorbance of the pure compound to measured pressures within the pressure range of the experiments, as described previously [45].

The experimental apparatus and sample preparation procedure have been reported previously [40]. The catalysts were reduced three times under 30 Torr of H₂ for 0.5 h at 723 K, and the reaction chamber was evacuated to below 6×10^{-7} Torr between each reduction. Following the reductions, CO₂ and H₂ were introduced into the reaction chamber at a total pressure of 13.0 Torr and a partial pressure ratio of 1 CO₂:3H₂. The FTIR spectra of gas-phase species were recorded as a function of time at 623 K for 2 h.

Reaction kinetics were modeled using a first order reaction for CO₂ consumption and deactivation kinetics, Eq. (E1), where X is the conversion, k_r is the first order reaction rate constant, k_d is the first order deactivation rate constant, and t is reaction time after the reactant gases are introduced [47]. The first order rate constants for the reaction over each catalyst were extracted using these models.

$$1 - X = e^{\frac{k_r}{k_d}(e^{-k_d t} - 1)} \quad (\text{E1})$$

3. Results and discussion

3.1. Catalyst characterization

3.1.1. Pulse CO chemisorption

The CO uptake values for all the catalysts are listed in Table 1. CO uptake values are typically correlated with the number of active metal sites for a given catalyst, but the complex interactions between the admetal and the CeO₂ support can potentially convolute the quantification of active sites. The relative values, though, show the average trend in the number of active sites for the catalysts, with the assumption

Table 1

Catalyst characterization by pulse CO chemisorption for Ni_xFe_y/CeO₂ catalysts. Metal loading corresponds to atomic ratios based on Pt atomic weight, consistent with previous work [39].

Catalysts	Metal loading (wt%)	CO uptake (μmol g cat ⁻¹)
Ni ₁	0.5% Ni	13.1
Ni ₂	1.0% Ni	16.9
Ni ₃	1.5% Ni	37.8
Ni ₁₀	5.0% Ni	39.7
Ni ₃ Fe ₁	1.5% Ni, 0.5% Fe	36.0
Ni ₃ Fe ₃	1.5% Ni, 1.4% Fe	32.2
Fe ₃	1.4% Fe	6.90

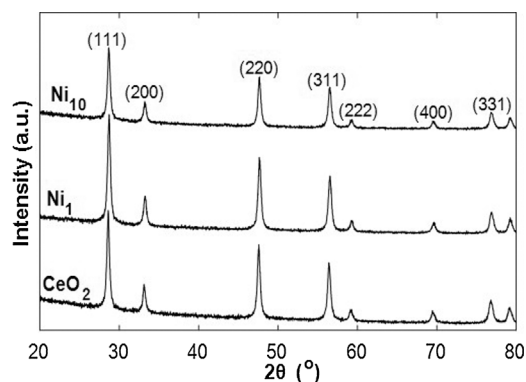


Fig. 2. XRD patterns of fresh 5% and 0.5% Ni/CeO₂ catalysts, and treated CeO₂.

that each adsorbed CO molecule corresponds to one metal active site.

For the Ni-only catalysts, the respective CO uptake values are 13.1, 16.9, 37.8, and 39.7 μmol g⁻¹ for 0.5%, 1.0%, 1.5%, and 5% Ni/CeO₂ (referred to as Ni₁, Ni₂, Ni₃, and Ni₁₀). The values increase with Ni loading up to 1.5%, as expected. However, the values do not rise significantly as the Ni loading is increased to 5%, suggesting that the Ni particles may agglomerate above 1.5% Ni loading.

For the Fe-containing catalysts, the CO uptake values increase with decreasing Fe content: 6.90, 32.2, 36.0, and 37.8 μmol g⁻¹ for Fe₃, Ni₃Fe₃, Ni₃Fe₁, and Ni₃, respectively (loading amounts of each admetal are detailed in Table 1). Despite the higher metal content of the bi-metallic catalysts, monometallic Ni₃ has the largest CO uptake value, and the CO uptake values of Ni-containing catalysts are substantially larger than that for monometallic Fe₃. These results indicate that Fe/CeO₂ contains fewer metallic sites than does Ni/CeO₂ for relatively low reduction temperatures (723 K).

3.1.2. Powder X-ray diffraction (XRD)

The XRD patterns obtained for the catalysts containing the highest and lowest Ni loading, and blank CeO₂ are shown in Fig. 2. These patterns are characteristic of fluorite CeO₂ nanoparticles (JCPDS 34-0394, space group Fm3m). No signals from Ni were detected, even for the sample with the highest metal loading (5% Ni). These results are consistent with the literature, where the particle sizes associated with Ni loading on CeO₂ below 10% are too small for detection by XRD [29,34].

3.1.3. High-resolution transmission electron microscopy (HR-TEM)

HR-TEM images and the corresponding particle size distributions for several Ni/CeO₂ catalysts are shown in Fig. 3. The images reveal that the Ni particles are smaller for Ni₁ than for the other three catalysts with higher loadings. The average diameter of Ni particles for Ni₁, Ni₂, Ni₃, and Ni₁₀ is 0.64(0.65) ± 0.12 nm, 1.11(1.06) ± 0.21 nm, 0.92(0.92) ± 0.19 nm, and 1.12(1.15) ± 0.17 nm, respectively (median diameter given in parenthesis). Even considering the substantial variation in particle sizes and inherent statistical uncertainty in the measurements due to poor contrast between the support and metal clusters, it can be concluded that Ni₁ catalyst particle sizes are significantly smaller than those of the other three Ni catalysts.

3.1.4. Temperature-programmed reduction (TPR)

The TPR results of Ni_xFe_y/CeO₂ are summarized in Fig. 4. Two major reduction peaks are observed for each catalyst in this series, corresponding to partial reductions of Ni and Fe oxides. The two peaks for the monometallic Ni catalyst correspond to reduction of NiO, and they are located at 474 and 531 K [34]. The major peaks for the monometallic Fe sample relate to the reduction of Fe₂O₃, located at 520 and 614 K. The presence of two peaks may correspond to complete, two-step reduction of the metals (NiO → Ni²⁺ → Ni⁰ and Fe₂O₃ → Fe₃O₄ → Fe⁰), but may also indicate incomplete partial reduction due

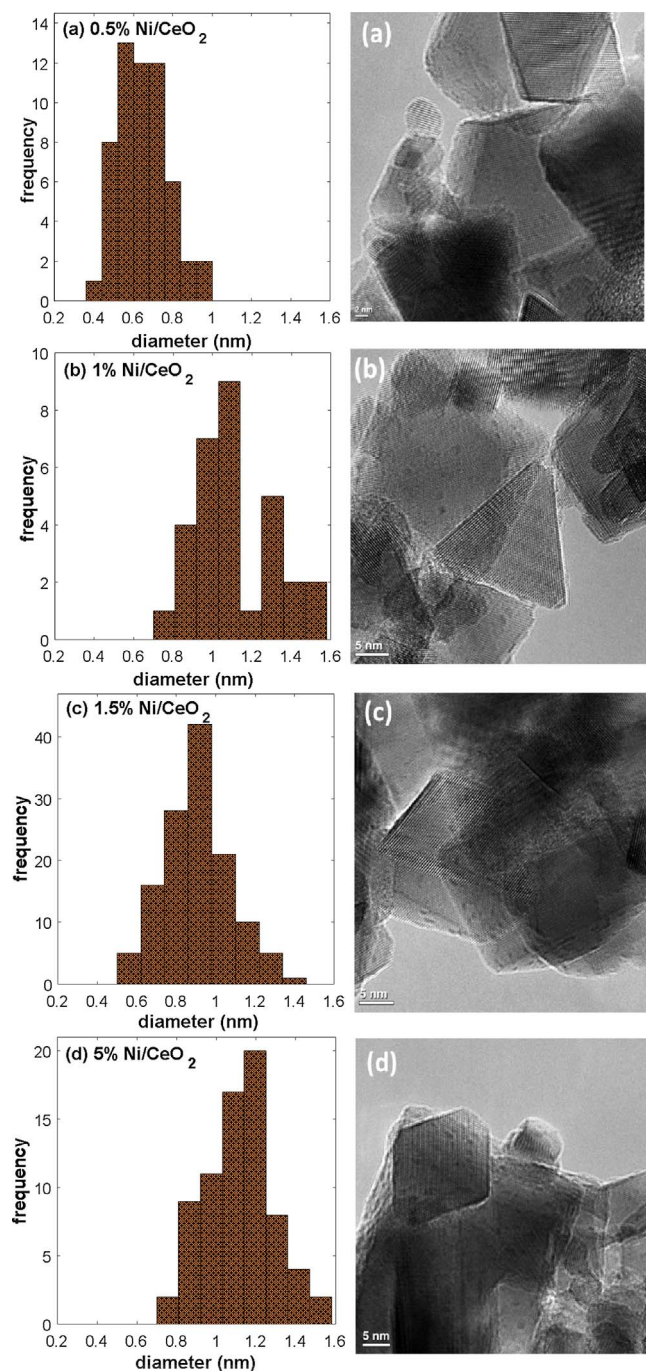


Fig. 3. TEM micrographs and particle size distributions for CeO₂-supported catalysts (a) Ni₁, (b) Ni₂, (c) Ni₃, and (d) Ni₁₀.

to variation in the phases present in the catalyst [34,48,49]. The extent of reduction of the metals is further elucidated in Section 3.1.5 using XANES.

The TPR profiles of the two bimetallic catalysts show desorption peaks occurring at temperatures between those of the monometallic Ni and Fe catalysts. The observation that the peak temperatures of the bimetallic catalysts are different from those of either Ni or Fe suggests bimetallic interactions in the Ni₃Fe₁ and Ni₃Fe₃ catalysts. Similarly, the CO uptake values decrease slightly with addition of Fe to Ni/CeO₂ catalysts. This suggests that the nanostructure of the catalyst is affected by the addition of Fe.

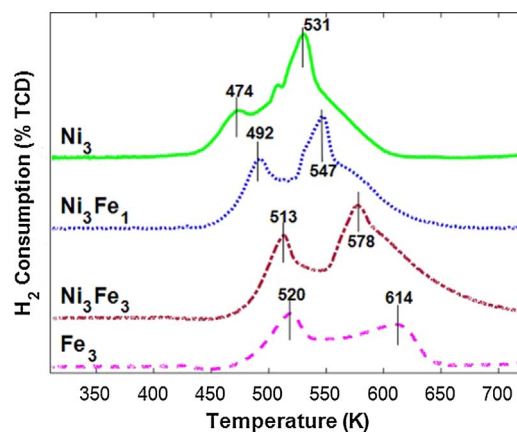


Fig. 4. H₂-TPR profiles of CeO₂-supported Fe₃, Ni₃Fe₁, Ni₃Fe₃, and Ni₃ catalysts. Samples were reduced at a heating rate of 14 K min⁻¹ with a flow rate of 20 mL min⁻¹ of 10% H₂ in Ar.

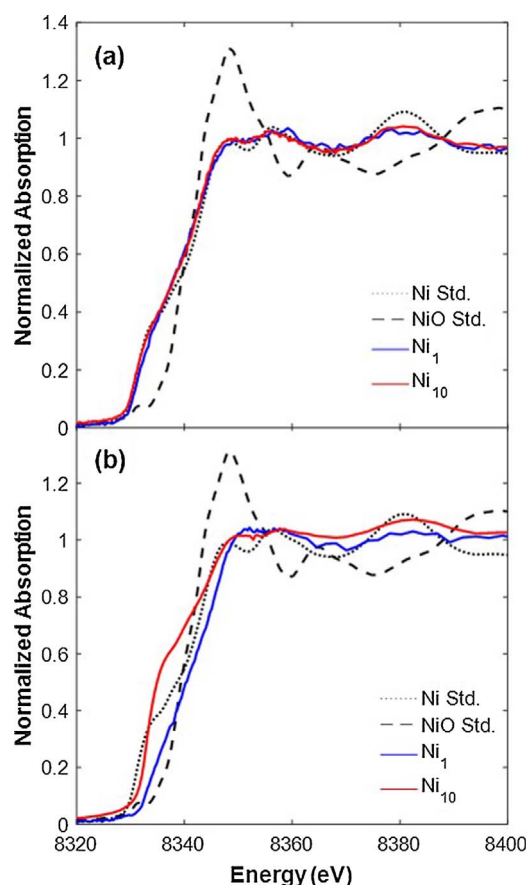


Fig. 5. Ni K-edge XANES spectra for Ni₁ and Ni₁₀ catalysts (a) reduced in H₂ and (b) under reaction conditions of 3 H₂:1 CO₂. Spectra for metallic Ni and NiO standards are included as references.

3.1.5. X-ray absorption near edge spectroscopy (XANES)

The Ni K-edge XANES spectra for reduced Ni/CeO₂ catalysts are shown with metallic and oxidized Ni standards in Fig. 5a. The *in situ* spectra under 3 H₂:1 CO₂ at 623 K for these catalysts are given in Fig. 5b. Comparison of the edge jump peak heights of 0.5% and 5% Ni to the references suggests that Ni is in the metallic state under both reduction and reaction conditions.

In order to compare the oxidation states of the bimetallic catalysts, the Fe and Ni K-edge XANES spectra are shown along with reference spectra in Fig. 6. The Ni oxidation state in all the catalysts is metallic,

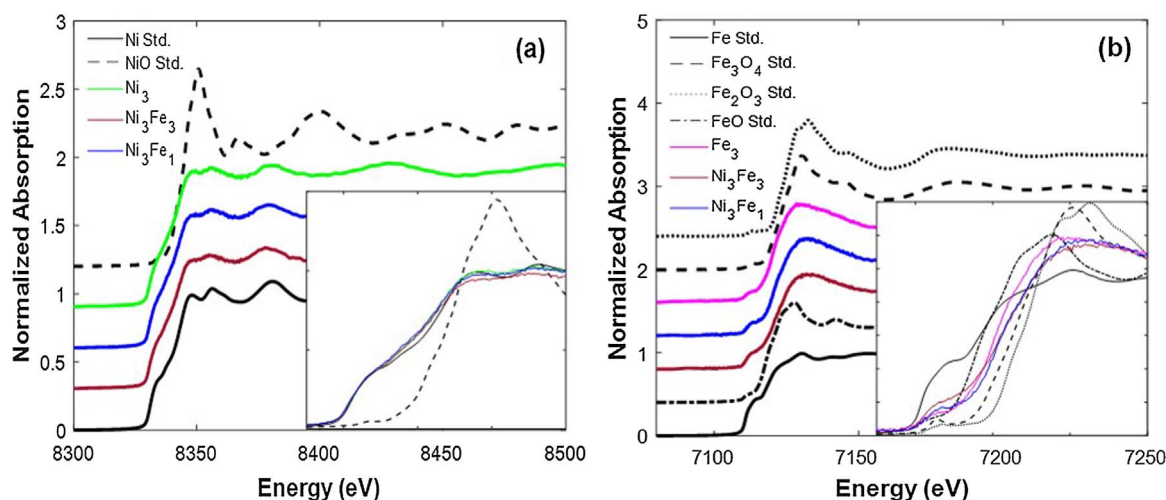


Fig. 6. XANES spectra of (a) the Ni K-edge for CeO_2 -supported Ni_3 , Ni_3Fe_3 , and Ni_3Fe_1 catalysts with metallic and oxidized Ni reference standards, and (b) the Fe K-edge for Fe_3 , Ni_3Fe_3 , and Ni_3Fe_1 catalysts with metallic and oxidized Fe reference standards. Insets focus on the near edge region with the pre-edge normalized to zero for all spectra.

based on the similarities to the metallic Ni reference standard in Fig. 6a.

The Fe K-edge XANES spectra in Fig. 6b reveal that the Fe-containing catalysts have a mixture of oxidation states. Based on the peak height of the absorption edges with respect to the reference standards, the oxidation state of Fe is roughly between Fe^{2+} and Fe^{3+} for all three Fe-containing catalysts. The linear combination fitting of the spectra to the reference standards is unsatisfactory, as shown in the Supporting Information. This poor fit suggests that $\text{FeO}_x/\text{CeO}_2$ has a special geometric structure (e.g. amorphous forms), since the pre-edge feature of Fe should be influenced both by the oxidation state and by the symmetry of the Fe coordination field.

The relative peak heights of the Fe absorption edges suggest that Fe in the bimetallic Ni_3Fe_1 and Ni_3Fe_3 catalysts is less oxidized than Fe in the monometallic Fe_3 catalyst. This result may be explained by the tendency of metallic Ni to enhance H_2 dissociation and to facilitate spillover of atomic hydrogen, which in turn promotes the reduction of Fe oxides in the Ni-Fe catalysts.

3.2. In situ FTIR spectroscopy reactor experiments

3.2.1. Ni loading and interactions with CeO_2 support

The ratios of the product gases CO/CH_4 measured over time for each catalyst are shown in Fig. 7a. For ease of comparing selectivity at the same conversion, the values of the CO/CH_4 ratios corresponding to an equal CO_2 conversion of 10% are indicated in the figure (in parentheses) and in Table 2. The CO/H_4 ratio decreases with Ni loading, with Ni_1 being strongly selective to CO.

The CO_2 hydrogenation activity increases with Ni loading, as illustrated in Fig. 7b. The final CO_2 conversions after 2 h of reacting at 623 K are 12%, 24%, 37%, and 47% for Ni_1 , Ni_2 , Ni_3 , and Ni_{10} , respectively. Similarly, the first order site-normalized rate constants are 0.122 , 0.218 , 0.269 , and $0.656 \times 10^{-3} \text{ min}^{-1} \mu\text{mol CO}^{-1}$, respectively. The agreement between the experimental data and the conversion profiles for the first 20 min of the reaction calculated using these rate constants is shown in Fig. 7b. The activity trend is in agreement with the literature, where CO_2 conversion increases with Ni loading on CeO_2 [29]. The trend is also consistent with the accepted mechanism for methanation: in a batch reactor, CO may function as an intermediate for CH_4 formation. The CO and CH_4 production rates shown in Fig. 7c-d are consistent with this mechanism. For all four catalysts, the rate of production of CO is rapid for the initial 5–10 min of the reaction, and the rate of production of CH_4 is much slower initially. For the strong methanation catalysts, Ni_3 and Ni_{10} , the CO turnover number (TON) begins to decrease after reacting for about 30 min while CH_4 production

continues to increase at a steady rate. The Ni_2 and Ni_1 catalysts produce more CO per active site than the catalysts containing larger amounts of Ni because of their lower methanation activity ($4.6 \times 10^{-4} \text{ mol CO L}^{-1} \text{ site}^{-1}$ for Ni_1), since less of the CO produced is converted to CH_4 .

Since XANES analysis identified Ni_1 as metallic, the strong CO selectivity of this catalyst with respect to those with higher loading is not driven by changes in Ni oxidation state. SMSIs and changes in Ni cluster sizes and dispersion on the support may account for this shift. For example, HR-TEM results (Fig. 3) indicate smaller Ni clusters in the Ni_1 catalyst compared to the other higher loading Ni catalysts. In order to confirm that the change in the CO/CH_4 ratio is not caused by the batch reactor configuration, atmospheric pressure flow reactor experiments were also performed for the Ni_1 and Ni_3 catalysts (see Supporting Information for flow reactor studies). The steady state ratio of CO/CH_4 yields in the flow reactor follows a similar trend to that in the batch reactor, decreasing from 0.68 for Ni_1 to 0.28 for Ni_3 .

The Ni metal loading effect may be explained by its influence on the adsorption strength of CO due to changing SMSIs. Partial electron transfer from the support to the active metal contributes to the anti-bonding π -orbital of adsorbed CO and weakens the C=O bond in addition to enhancing hydrogen dissociation on the active metal, dually promoting methanation [23,50]. DFT analysis has revealed an opening of Ni particles when deposited on CeO_2 -(111), leading to the formation of more active surface sites [51]. Theoretical and experimental investigations by Carrasco et al. have confirmed the higher C–O bond strength of adsorbed CO on highly dispersed, low loading of Ni/CeO_2 compared to higher loading or agglomerated Ni particles and metallic Ni-(111) surfaces. The low methanation activity for low loading Ni/CeO_2 catalysts may be explained by these SMSIs, which allow the C–O bond strength of adsorbed CO to remain sufficiently high to prevent dissociation and subsequent methanation.

The trends in activity and selectivity in Fig. 7 were used to select a Ni/CeO_2 catalyst to modify with Fe. Since significant methanation occurs over Ni/CeO_2 at a metal loading of 1.5% (Ni_3), Ni_3Fe_x bimetallic catalysts were used to enhance CO selectivity while maintaining high CO_2 conversion activities.

3.2.2. Fe modification of 1.5% Ni/CeO_2 catalysts

The batch reactor results of CO_2 hydrogenation over Ni-Fe catalysts are summarized in Fig. 8. The monometallic Fe catalyst is 100% selective to CO and the monometallic Ni catalyst has the lowest CO selectivity. For the two bimetallic catalysts, the CO/CH_4 product ratio increases with Fe content. The values of the product ratios at 10% CO_2 conversion are indicated in Fig. 8a (in parentheses) and listed in

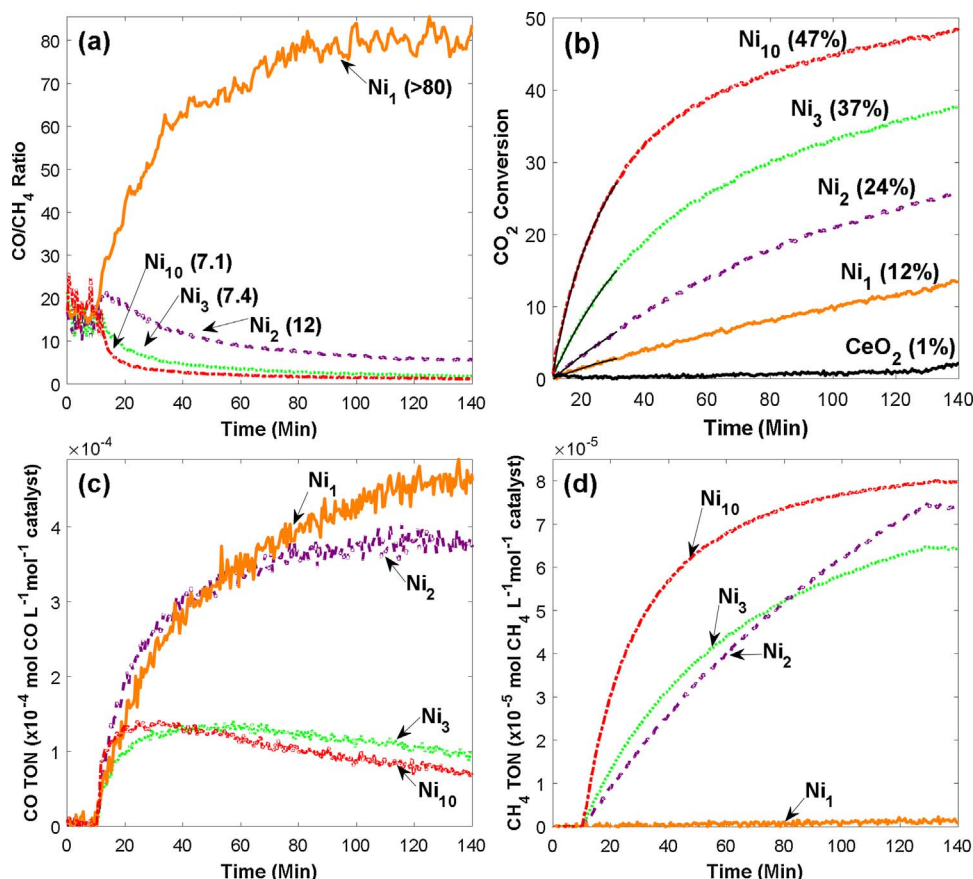


Fig. 7. The reduction of CO_2 by H_2 at 623 K for a series of Ni_x/CeO_2 catalysts with increasing loading amounts x of Ni. (a) The ratio of CO/CH_4 produced, (b) the consumption of CO_2 , (c) the production of CO , and (d) the production of CH_4 over time. The value of the CO/CH_4 ratio at 10% CO_2 conversion is indicated in (a). The fit of the conversion profile using calculated rate constants for first order reaction and deactivation kinetics for the initial 20 min of reaction are shown for each Ni_x/CeO_2 catalyst in (b), where the reaction begins at 10 min.

Table 2

First-order consumption rate constants and product ratios for CO_2 conversion by H_2 for Ni_x/CeO_2 catalysts. Rate constants are normalized by catalyst weight and CO uptake values. Product ratios are evaluated at 10% CO_2 conversion.

Catalyst	k_r 1st order ($\times 10^{-3} \text{ min}^{-1} \text{ gcat}^{-1}$)	Normalized k_r ($\times 10^{-3} \text{ min}^{-1} \mu\text{mol CO}^{-1}$)	CO/CH_4 ratio at 10% conversion
Ni_1	1.60	0.122	> 80
Ni_2	3.68	0.218	12
Ni_3	10.2	0.269	7.4
Ni_{10}	26.0	0.656	7.1

Table 3: > 80, 19, 14, and 7.4 for Fe_3 , Ni_3Fe_3 , Ni_3Fe_1 , and Ni_3 , respectively.

The monometallic Fe catalyst is the least active, with a final CO_2 conversion of 8.3% and first order rate constant of $0.110 \times 10^{-3} \text{ min}^{-1} \mu\text{mol CO}^{-1}$. The activity of the bimetallic catalysts increases with decreasing Fe content, with final CO_2 conversions of 27%, 29%, and 37% (Fig. 8b), and first order rate constants of 0.162, 0.268, and $0.269 \times 10^{-3} \text{ min}^{-1} \mu\text{mol CO}^{-1}$ for Ni_3Fe_3 , Ni_3Fe_1 , and Ni_3 , respectively. Notably, the activity of Ni_3Fe_1 is comparable to that of Ni_3 based on the first order rate constants, indicating a smaller dampening effect by Fe on Ni activity for this reaction, despite the substantial enhancement in CO selectivity for the Ni_3Fe_1 catalyst. Since Fe oxide is known to form solid solutions with CeO_2 , the introduction of Fe cations into the support lattice may affect the interaction with CO_2 [48,52].

The Fe_3 catalyst produces significant amounts of CO per active site despite its low activity, due to the lack of methanation activity for this catalyst. The equimolar Ni-Fe catalyst, Ni_3Fe_3 , represents an optimization of the activity provided by Ni/CeO_2 and the CO selectivity characteristic of Fe/CeO_2 . This catalyst shows an enhanced CO TON compared to Ni_3 , and it has remarkably greater activity than the

monometallic Fe catalyst based on both CO_2 conversion and first order rate constants.

The XANES characterization results reveal the presence of partially oxidized Fe while Ni remains metallic. The interaction of Fe and Fe oxides with Ni and CeO_2 changes the properties of the catalysts in favor of CO selectivity. For example, the presence of Fe oxides may decrease the affinity of the surface for CO, leading to CO desorption instead of subsequent methanation.

DFT calculations have provided a correlation between CO binding energy and product selectivity for the CO_2 hydrogenation reaction over supported metal catalysts. Synergy between metals and supports can achieve intermediate interaction strengths of active sites with adsorbates to improve reaction selectivity [17,53]. Additionally, CO methanation has been demonstrated to follow a volcano relation using CO adsorption energy as the descriptor, with Ni and Fe situated on opposite sides of the volcano peak [54]. The combination of these metals on CeO_2 may represent a synergy of their electronic properties, leading to an intermediate affinity for CO that is strong enough to enable high CO_2 dissociation activity, yet weak enough to allow for desorption of CO without further hydrogenation to CH_4 . However, the bimetallic Ni-Fe catalysts under consideration here contain mostly oxidized Fe, so DFT calculations of metallic Ni-Fe systems are unsatisfactory for explaining the unique properties of these catalysts. More in-depth theoretical and experimental studies are needed regarding the interactions among Fe oxides, metallic Fe, metallic Ni, and the reducible metal oxide support in order to explain the observed trends in activity and selectivity.

4. Conclusions

Results from the current study provide an understanding of the effects of Ni loading and Fe/FeO_x modification on the activity and selectivity of CO_2 hydrogenation over Ni/CeO_2 catalysts. With low Ni loading, Ni/CeO_2 is highly selective to CO but the CO_2 conversion is

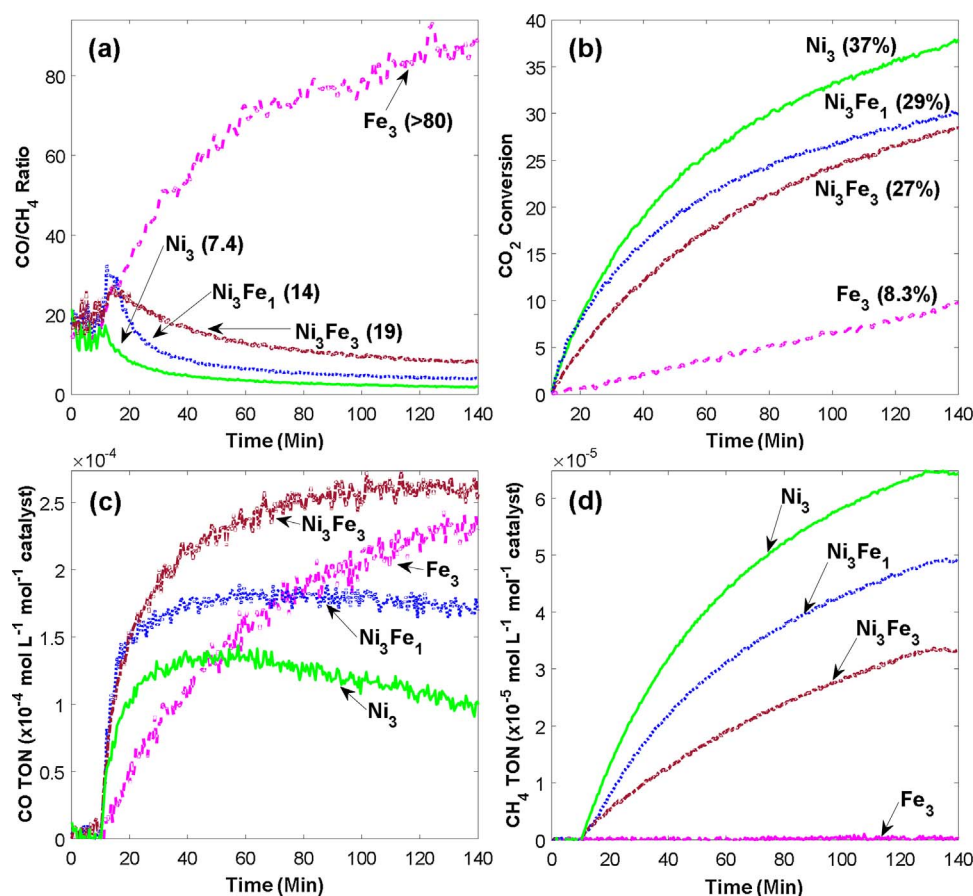


Fig. 8. The reduction of CO_2 by H_2 at 623 K for a series of $\text{Ni}_x\text{Fe}_y/\text{CeO}_2$ catalysts with increasing loading amounts x of Ni. (a) The ratio of CO/CH_4 produced, (b) the consumption of CO_2 , (c) the production of CO , and (d) the production of CH_4 over time. The value of the CO/CH_4 ratio at 10% CO_2 conversion is indicated in (a).

Table 3

First-order consumption rate constants and product ratios for CO_2 conversion by H_2 for $\text{Ni}_x\text{Fe}_y/\text{CeO}_2$ catalysts. Rate constants are normalized by catalyst weight and CO uptake values. Product ratios are evaluated at 10% CO_2 conversion.

Catalysts	k_r 1st order ($\times 10^{-3} \text{ min}^{-1} \text{ gcat}^{-1}$)	Normalized k_r ($\times 10^{-3} \text{ min}^{-1} \mu\text{mol CO}^{-1}$)	CO/CH_4 ratio at 10% conversion
Fe_3	0.760	0.110	> 80
Ni_3Fe_3	5.21	0.162	19
Ni_3Fe_1	9.64	0.268	14
Ni_3	10.2	0.269	7.4

low; high metal loading of Ni/CeO_2 has higher activity but is selective to CH_4 .

The catalyst with 0.5% Ni was highly selective to CO compared to catalysts with higher Ni loading. The activity followed an inverse trend to CO selectivity, as summarized in Fig. 9a. This trend has been

previously attributed to the presence of oxidized Ni, but XANES analysis in the current study revealed that the CO -selective 0.5% Ni catalyst contained Ni in the metallic state. This suggests that metal-support interactions and metal cluster sizes and distributions may account for the observed shift in selectivity with metal loading. The trend in selectivity may be explained by the stronger C–O bond strength of adsorbed CO on low loading Ni/CeO_2 compared to higher loading and metallic Ni surfaces.

The co-impregnation of Fe with 1.5% Ni in a 3:1 molar ratio of Ni to Fe resulted in comparable activity to the monometallic Ni catalyst but improved CO selectivity. Using a 1:1 ratio of Ni to Fe further improved the selectivity – although reduced the catalyst activity (Fig. 9b) – and yielded a higher CO turnover number with respect to the parent metals. Based on XANES absorption edge peak heights, a significant amount of Fe in the bimetallic catalysts remained oxidized. In the bimetallic catalysts, Ni contributed to the reduction of Fe oxides via enhancing H_2 dissociation and hydrogen spillover to the Fe oxides, as evidenced by

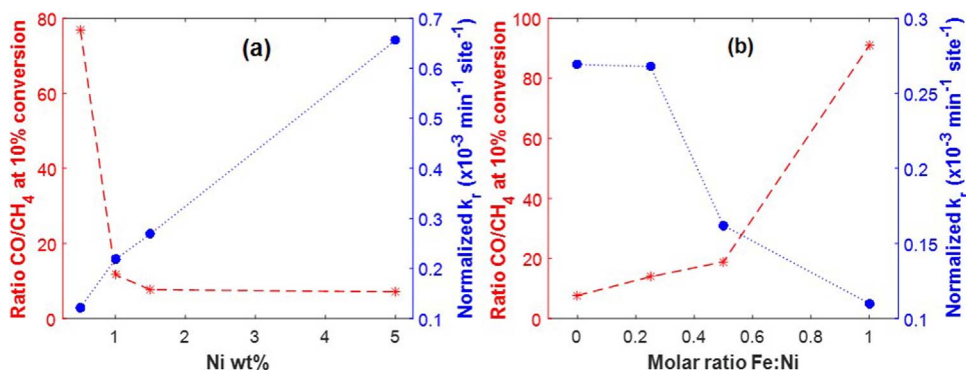


Fig. 9. Summary of activity based on reaction rate constants normalized by catalyst mass and number of active sites, and selectivity based on the ratio of CO/CH_4 produced at the time of 10% conversion of CO_2 by H_2 , for (a) Ni_x/CeO_2 catalysts and (b) $\text{Ni}_x\text{Fe}_y/\text{CeO}_2$ catalysts.

TPR, CO chemisorption, and XANES. The presence of Fe oxides may weaken the binding strength of the catalysts, enabling more facile CO desorption. Since CO was observed to serve as an intermediate to formation of CH₄ from CO₂, the reduced adsorption strength of CO may decrease the extent to which adsorbed CO is hydrogenated to CH₄. More in-depth DFT calculations are needed to understand the interactions among Fe oxides, metallic Fe, metallic Ni, and the reducible CeO₂ support and the corresponding effects on the CO₂ hydrogenation activity and selectivity.

Acknowledgements

The work is supported by the US Department of Energy (DE-SC0012704). LW acknowledges the US National Science Foundation Graduate Research Fellowship Program grant number DGE 16-44869. We thank Mr. Qiyuan Wu for collecting TEM images.

Appendix A. Supplementary data

Supplementary data associated with this article can be found, in the online version, at <http://dx.doi.org/10.1016/j.apcatb.2017.10.036>.

References

- [1] T.R. Knutson, R.E. Tuleya, Impact of CO₂-induced warming on simulated hurricane intensity and precipitation: sensitivity to the choice of climate model and convective parameterization, *J. Clim.* 17 (2004) 3477–3495.
- [2] J. Hansen, M. Sato, R. Ruedy, K. Lo, D.W. Lea, M. Medina-Elizade, Global temperature change, *PNAS* 103 (2006) 14288–14293.
- [3] EPA, FACT SHEET: Clean Power Plan Overview, EPA Clean Power Plan, (2014) <https://www.epa.gov/sites/production/files/2014-05/documents/20140602fs-overview.pdf> (Accessed 22 December 2016).
- [4] J.N. Farrell, Cleaning up America's coal: an analysis of states' potentials for carbon capture and storage, *Intersect Stanford J. Sci. Technol. Soc.* 9 (2015) 1–21.
- [5] S.C. Doney, V.J. Fabry, R.A. Feely, J.A. Kleypas, Ocean acidification: the other CO₂ problem, *Annu. Rev. Mar. Sci.* 1 (2009) 169–192, <http://dx.doi.org/10.1146/annurev.marine.010908.163834>.
- [6] G. Centi, S. Perathoner, Opportunities and prospects in the chemical recycling of carbon dioxide to fuels, *Catal. Today* 148 (2009) 191–205, <http://dx.doi.org/10.1016/j.cattod.2009.07.075>.
- [7] S. Perathoner, G. Centi, CO₂ recycling: a key strategy to introduce green energy in the chemical production chain, *ChemSusChem* 7 (2014) 1274–1282, <http://dx.doi.org/10.1002/cssc.201300926>.
- [8] U.S. Energy Information Administration, International Energy Outlook 2016, (2016) [www.eia.gov/forecasts/ieo/pdf/0484\(2016\).pdf](http://www.eia.gov/forecasts/ieo/pdf/0484(2016).pdf).
- [9] G. Centi, S. Perathoner (Eds.), *Green Carbon Dioxide: Advances in CO₂ Utilization*, John Wiley & Sons, Hoboken, NJ, 2014.
- [10] M.D. Porosoff, B. Yan, J.G. Chen, Catalytic reduction of CO₂ by H₂ for synthesis of CO, methanol and hydrocarbons: challenges and opportunities, *Energy Environ. Sci.* 9 (2016) 62–73, <http://dx.doi.org/10.1039/C5EE02657A>.
- [11] M.D. Porosoff, W. Yu, J.G. Chen, Challenges and opportunities in correlating bimetallic model surfaces and supported catalysts, *J. Catal.* 308 (2013) 2–10, <http://dx.doi.org/10.1016/j.jcat.2013.05.009>.
- [12] C.-S. Chen, W.-H. Cheng, S.-S. Lin, Mechanism of CO formation in reverse water-gas shift reaction over Cu/Al₂O₃ catalyst, *Catal. Lett.* 68 (2000) 45–48.
- [13] X. Wang, H. Shi, J.H. Kwak, J. Szanyi, Mechanism of CO₂ hydrogenation on Pd/Al₂O₃ catalysts: kinetics and transient DRIFTS-MS studies, *ACS Catal.* 5 (2015) 6337–6349, <http://dx.doi.org/10.1021/acscatal.5b01464>.
- [14] W.C. Conner, J.L. Falconer, Spillover in heterogeneous catalysis, *Chem. Rev.* 95 (1995) 759–708.
- [15] C.-S. Chen, W.-H. Cheng, S.-S. Lin, Study of reverse water gas shift reaction by TPD, TPR and CO₂ hydrogenation over potassium-promoted Cu/SiO₂ catalyst, *Appl. Catal. A Gen.* 238 (2003) 55–67.
- [16] J.A. Rodriguez, P. Liu, D.J. Stachchiola, S.D. Senanayake, M.G. White, J.G. Chen, Hydrogenation of CO₂ to methanol: importance of metal-oxide and metal-carbide interfaces in the activation of CO₂, *ACS Catal.* 5 (2015) 6696–6706, <http://dx.doi.org/10.1021/acscatal.5b01755>.
- [17] S. Kattel, B. Yan, Y. Yang, J.G. Chen, P. Liu, Optimizing binding energies of key intermediates for CO₂ hydrogenation to methanol over oxide-supported copper, *J. Am. Chem. Soc.* 138 (2016) 12440–12450, <http://dx.doi.org/10.1021/jacs.6b05791>.
- [18] J.L. Falconer, A.E. Zagli, Adsorption and methanation of carbon dioxide on a nickel/silica catalyst, *J. Catal.* 62 (1980) 280–285.
- [19] G.D. Weatherbee, C.H. Bartholomew, Hydrogenation of CO₂ on group VIII metals II. kinetics and mechanism of CO₂ hydrogenation on nickel, *J. Catal.* 77 (1982) 460–472 N.
- [20] M. Marwood, R. Doepper, A. Renken, In-situ surface and gas phase analysis for kinetic studies under transient conditions The catalytic hydrogenation of CO₂, *Appl. Catal. A Gen.* 151 (1997) 223–246.
- [21] A.L. Lapidus, N.A. Gaidai, N.V. Nekrasov, L.A. Tishkova, Y.A. Agafonov, T.N. Myshechkova, The mechanism of carbon dioxide hydrogenation on copper and nickel catalysts, *Pet. Chem.* 47 (2007) 75–82.
- [22] J. Sehested, S. Dahl, J. Jacobsen, J.R. Rostrup-Nielsen, Methanation of CO over nickel: mechanism and kinetics at high H₂/CO ratios, *J. Phys. Chem. B* 109 (2005) 2432–2438, <http://dx.doi.org/10.1021/jp040239s>.
- [23] S. Tada, T. Shimizu, H. Kameyama, T. Haneda, R. Kikuchi, Ni/CeO₂ catalysts with high CO₂ methanation activity and high CH₄ selectivity at low temperatures, *Int. J. Hydrogen Energy* 37 (2012) 5527–5531, <http://dx.doi.org/10.1016/j.ijhydene.2011.12.122>.
- [24] T. Staudt, Y. Lykhach, N. Tsud, T. Skála, K.C. Prince, V. Matolín, J. Libuda, Ceria reoxidation by CO₂: a model study, *J. Catal.* 275 (2010) 181–185, <http://dx.doi.org/10.1016/j.jcat.2010.07.032>.
- [25] A. Trovarelli, C. Deleitenburg, G. Dolcetti, J.L. Lorca, CO₂ methanation under transient and steady-state conditions over Rh/CeO₂ and CeO₂-promoted Rh/SiO₂: the role of surface and bulk ceria, *J. Catal.* 151 (1995) 111–124, <http://dx.doi.org/10.1006/jcat.1995.1014>.
- [26] T. Odedairo, J. Chen, Z. Zhu, Synthesis of supported nickel nanoparticles via a nonthermal plasma approach and its application in CO₂ reforming of methane, *J. Phys. Chem. C* 117 (2013) 21288–21302, <http://dx.doi.org/10.1021/jp405009v>.
- [27] B. Lu, K. Kawamoto, Preparation of the highly loaded and well-dispersed NiO/SBA-15 for methanation of producer gas, *RSC Adv.* 2 (2012) 6800–6805, <http://dx.doi.org/10.1016/j.fuel.2012.09.009>.
- [28] B. Lu, K. Kawamoto, Preparation of monodispersed NiO particles in SBA-15, and its enhanced selectivity for reverse water gas shift reaction, *J. Environ. Chem. Eng.* 1 (2013) 300–309, <http://dx.doi.org/10.1016/j.jeece.2013.05.008>.
- [29] B. Lu, K. Kawamoto, Preparation of mesoporous CeO₂ and monodispersed NiO particles in CeO₂, and enhanced selectivity of NiO/CeO₂ for reverse water gas shift reaction, *Mater. Res. Bull.* 53 (2014) 70–78, <http://dx.doi.org/10.1016/j.materresbull.2014.01.043>.
- [30] J. Carrasco, L. Barrio, P. Liu, J.A. Rodriguez, M.V. Ganduglia-Pirovano, Theoretical studies of the adsorption of CO and C on Ni(111) and Ni/CeO₂(111): evidence of a strong metal-support interaction, *J. Phys. Chem. C* 117 (2013) 8241–8250, <http://dx.doi.org/10.1021/jp400430r>.
- [31] S.D. Senanayake, J. Evans, S. Agnoli, L. Barrio, T.L. Chen, J. Hrbek, J.A. Rodriguez, Water-gas shift and CO methanation reactions over Ni-CeO₂(111) catalysts, *Top. Catal.* 54 (2011) 34–41, <http://dx.doi.org/10.1007/s11244-011-9645-6>.
- [32] T. Shido, Y. Iwasawa, Regulation of reaction intermediate by reactant in the water-gas shift reaction on CeO₂, in relation to reactant-promoted mechanism, *J. Catal.* 136 (1992) 493–503, [http://dx.doi.org/10.1016/0021-9517\(92\)90079-W](http://dx.doi.org/10.1016/0021-9517(92)90079-W).
- [33] G. Jacobs, E. Chenu, P.M. Patterson, L. Williams, D. Sparks, G. Thomas, B.H. Davis, Water-gas shift: comparative screening of metal promoters for metal/ceria systems and role of the metal, *Appl. Catal. A Gen.* 258 (2004) 203–214, <http://dx.doi.org/10.1016/j.apcata.2003.09.007>.
- [34] W. Shan, M. Luo, P. Ying, W. Shen, C. Li, Reduction property and catalytic activity of Ce₁-XNiO₂ mixed oxide catalysts for CH₄ oxidation, *Appl. Catal. A Gen.* 246 (2003) 1–9, [http://dx.doi.org/10.1016/S0926-860X\(02\)00659-2](http://dx.doi.org/10.1016/S0926-860X(02)00659-2).
- [35] Y. Zhou, J.M. Perket, A.B. Crooks, J. Zhou, Effect of ceria support on the structure of Ni nanoparticles, *J. Phys. Chem. Lett.* 1 (2010) 1447–1453, <http://dx.doi.org/10.1021/jz100304a>.
- [36] R.K. Singha, A. Shukla, A. Yadav, L.N. Sivakumar Konathala, R. Bal, Effect of metal-support interaction on activity and stability of Ni-CeO₂ catalyst for partial oxidation of methane, *Appl. Catal. B Environ.* 202 (2017) 473–488, <http://dx.doi.org/10.1016/j.apcatb.2016.09.060>.
- [37] N.M. Deraz, Effect of NiO content on structural, surface and catalytic characteristics of nano-crystalline NiO/CeO₂ system, *Ceram. Int.* 38 (2012) 747–753, <http://dx.doi.org/10.1016/j.ceramint.2011.07.068>.
- [38] P. Kumar, R. Idem, A comparative study of copper-promoted water-gas-shift (WGS) catalysts, *Energy Fuels* 21 (2007) 522–529, <http://dx.doi.org/10.1021/ef060389x>.
- [39] S. Lu, W.W. Lonergan, J.P. Bosco, S. Wang, Y. Zhu, Y. Xie, J.G. Chen, Low temperature hydrogenation of benzene and cyclohexene: a comparative study between γ-Al₂O₃ supported PtCo and PtNi bimetallic catalysts, *J. Catal.* 259 (2008) 260–268, <http://dx.doi.org/10.1016/j.jcat.2008.08.016>.
- [40] W.W. Lonergan, D.G. Vlachos, J.G. Chen, Correlating extent of Pt-Ni bond formation with low-temperature hydrogenation of benzene and 1,3-butadiene over supported Pt/Ni bimetallic catalysts, *J. Catal.* 271 (2010) 239–250, <http://dx.doi.org/10.1016/j.jcat.2010.01.019>.
- [41] S. Lu, W.W. Lonergan, Y. Zhu, Y. Xie, J.G. Chen, Support effect on the low-temperature hydrogenation of benzene over PtCo bimetallic and the corresponding monometallic catalysts, *Appl. Catal. B Environ.* 91 (2009) 610–618, <http://dx.doi.org/10.1016/j.apcatb.2009.06.036>.
- [42] J. Arenas-Alatorre, M. Avalos-Borja, G. Diaz, Microstructural characterization of bimetallic Ni-Pt catalysts supported on SiO₂, *Appl. Surf. Sci.* 189 (2002) 7–17.
- [43] S. Qi, B.A. Cheney, R. Zheng, W.W. Lonergan, W. Yu, J.G. Chen, The effects of oxide supports on the low temperature hydrogenation activity of acetone over Pt/Ni bimetallic catalysts on SiO₂, γ-Al₂O₃ and TiO₂, *Appl. Catal. A Gen.* 393 (2010) 44–49, <http://dx.doi.org/10.1016/j.apcata.2010.11.023>.
- [44] R. Zheng, M.P. Humbert, Y. Zhu, J.G. Chen, Low-temperature hydrogenation of the CQO bond of propanal over Ni-Pt bimetallic catalysts: from model surfaces to supported catalysts, *Catal. Sci. Technol. Catal. Sci. Technol.* 1 (2011) 638–643, <http://dx.doi.org/10.1039/c1cy00066g>.
- [45] M.D. Porosoff, J.G. Chen, Trends in the catalytic reduction of CO₂ by hydrogen over supported monometallic and bimetallic catalysts, *J. Catal.* 301 (2013) 30–37, <http://dx.doi.org/10.1016/j.jcat.2013.01.022>.
- [46] M.D. Porosoff, M.N.Z. Myint, S. Kattel, Z. Xie, E. Gomez, P. Liu, J.G. Chen,

- Identifying different types of catalysts for CO₂ reduction by ethane through dry reforming and oxidative dehydrogenation, *Angew. Chem. Int. Ed.* 54 (2015) 15501–15505, <http://dx.doi.org/10.1002/anie.201508128>.
- [47] H.S. Fogler, *Elements of Chemical Reaction Engineering*, 4th ed., Pearson Education Inc., Upper Saddle River, NJ, 2006, pp. 707–717.
- [48] A.S. Reddy, C. Chen, C. Chen, S. Chien, C. Lin, K. Lin, C. Chen, S. Chang, Synthesis and characterization of Fe/CeO₂ catalysts: epoxidation of cyclohexene, *J. Mol. Catal. A Chem.* 318 (2010) 60–67, <http://dx.doi.org/10.1016/j.molcata.2009.11.008>.
- [49] G. Neri, A. Pistone, C. Milone, S. Galvagno, Wet air oxidation of p-coumaric acid over promoted ceria catalysts, *Appl. Catal. B Environ.* 38 (2002) 321–329, [http://dx.doi.org/10.1016/S0926-3373\(02\)00061-9](http://dx.doi.org/10.1016/S0926-3373(02)00061-9).
- [50] B. Nematollahi, M. Rezaei, E.N. Lay, Selective methanation of carbon monoxide in hydrogen rich stream over Ni/CeO₂ nanocatalysts, *J. Rare Earths* 33 (2015) 619–628, [http://dx.doi.org/10.1016/S1002-0721\(14\)60462-2](http://dx.doi.org/10.1016/S1002-0721(14)60462-2).
- [51] K.R. Hahn, A.P. Seitsonen, M. Iannuzzi, J. Hutter, Functionalization of CeO₂(111) by deposition of small Ni clusters: effects on CO₂ adsorption and O vacancy formation, *ChemCatChem* 7 (2015) 625–634, <http://dx.doi.org/10.1002/cctc.201402906>.
- [52] F.J. Perez-Alonso, M. Lopez Granados, M. Ojeda, P. Terreros, S. Rojas, T. Herranz, J.L.G. Fierro, Chemical structures of coprecipitated Fe – Ce mixed oxides, *Chem. Mater.* 17 (2005) 2329–2339.
- [53] X. Yang, S. Kattel, S.D. Senanayake, J.A. Boscoboinik, X. Nie, J. Graciani, J.A. Rodriguez, P. Liu, D.J. Stacchiola, J.G. Chen, Low pressure CO₂ hydrogenation to methanol over gold nanoparticles activated on a CeO_x/TiO₂ interface, *J. Am. Chem. Soc.* 137 (2015) 10104–10107, <http://dx.doi.org/10.1021/jacs.5b06150>.
- [54] T. Bligaard, J.K. Nørskov, S. Dahl, J. Matthiesen, C.H. Christensen, J. Sehested, The Brønsted-Evans-Polanyi relation and the volcano curve in heterogeneous catalysis, *J. Catal.* 224 (2004) 206–217, <http://dx.doi.org/10.1016/j.jcat.2004.02.034>.